Article

Photodegradation of Riboflavin under Alkaline Conditions: What can Gas-Phase Photolysis Tell Us About What Happens in Solution?

Natalie G. K. Wong [1], Chris Rhodes [1] and Caroline E. H. Dessent [1,*]

[1] Department of Chemistry, University of York, Heslington, YO10 5DD, U.K.

* Correspondence: caroline.dessent@york.ac.uk; Tel.: +44 (0)1904-324092.

Abstract: The application of electrospray ionization mass spectrometry (ESI-MS) as a direct method for detecting reactive intermediates is a technique of developing importance in the routine monitoring of solution-phase reaction pathways. Here, we utilize a novel on-line photolysis ESI-MS approach to detect the photoproducts of riboflavin in aqueous solution under mildly alkaline conditions. Riboflavin is a constituent of many food products, so its breakdown processes are of wide interest. Our on-line photolysis setup allows for solution-phase photolysis to occur within a syringe using UVA LEDs, immediately prior to being introduced into the mass spectrometer *via* ESI. Gas-phase photofragmentation studies *via* laser-interfaced mass spectrometry of deprotonated riboflavin, [RF−H]⁻, the dominant solution-phase species under the conditions of our study, are presented alongside the solution-phase photolysis. The results obtained illustrate the extent to which gas-phase photolysis methods can inform our understanding of the corresponding solution-phase photochemistry. We determine that the solution-phase photofragmentation observed for [RF−H]⁻ closely mirrors the gas-phase photochemistry, with the *m/z* 241 ion being the only major condensed-phase photoproduct. Further gas-phase photoproducts are observed at *m/z* 255, 212, and 145. The value of exploring both the gas- and solution-phase photochemistry to characterize photochemical reactions is discussed.

Keywords: laser spectroscopy; online photolysis; solution-phase photolysis; vitamin; flavins; mass spectrometry

1. Introduction

Riboflavin (RF; Scheme 1) is one of the most well-studied members of the flavin family and is a vital water-soluble vitamin (B₂) naturally found in a wide range of food products (*e.g.,* milk, cheese, and green vegetables) and fortified foods (*e.g.,* cereals, bread, and beer). As a precursor of all biologically-significant flavins, riboflavin is an integral component of the (flavo)coenzymes flavin adenine dinucleotide (FAD) and flavin mononucleotide (FMN), both of which are active within several critical metabolic enzyme reactions.

Riboflavin shows broad absorption across the UV-visible regions in aqueous solution and has been observed to photodegrade *via* intramolecular and/or intermolecular photoreduction, photoaddition, and photodealkylation mechanisms to form an array of photoproducts including formylmethylflavin (FMF), lumichrome (LC), lumiflavin (LF), carboxymethylflavin (CMF), cyclodehydroriboflavin (CDRF), and 2,3-butanedione, as reviewed in detail elsewhere [1]. These studies have revealed that the formation of intermediates is heavily dependent on reaction conditions (*i.e.*, pH, solvent, and light intensity), and that the intermediates have the capacity to degrade into secondary products [1,2].
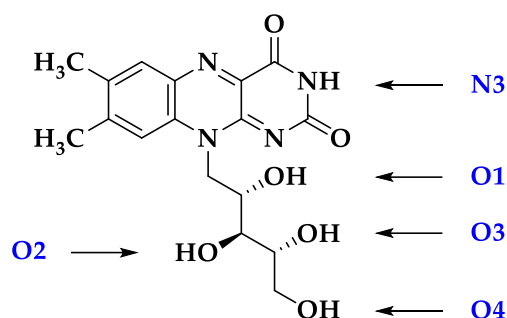
Scheme 1. Schematic diagram of the structure of riboflavin (RF). Typical labelling conventions have been applied to illustrate the possible deprotonation sites of a mono-anion deprotomer (*i.e.*, [RF–H]⁻).

In the body, riboflavin has an absorption maximum of *ca.* 447 nm. Human skin, which contains significant levels of riboflavin, can thereby photodegrade upon exposure to blue (visible) light, causing red-cell lysis and generalized tissue riboflavin deficiencies within the body. Earlier work on riboflavin has shown that it can act as an avid photosensitizer, yielding reactive oxygen species (ROS) such as the superoxide anion, hydroxy radical, hydrogen peroxide, as well as singlet oxygen. Such radicals can in turn promote the decomposition of other ingredients within food, pharmaceuticals, and cosmetics. Recent work investigating the influence of UV radiation on the RF photochemistry has shown that riboflavin directly produces singlet oxygen at 308, 330, 355, and 370 nm [3], explaining why riboflavin levels in food can rapidly degrade upon exposure to both natural and artificial light, thus limiting curbing its shelf-life. Given its prominence within many metabolic processes, it is of ongoing interest to better understand the photochemical breakdown pathways of riboflavin in order to develop better ways to stabilize the vitamin *in vivo* and within consumer products.

The condensed-phase photostability of riboflavin at various pH values (*i.e.*, (de)protonation state) has previously been addressed: under acidic/neutral conditions riboflavin photodegrades to LC whereas, under alkaline conditions, it photodissociates to both LC and LF. Whilst LC is formed *via* a riboflavin excited singlet state (¹RF*), both LF and LC can be formed *via* intramolecular photoreduction from an excited triplet state (³RF*). The pKₐ values of riboflavin are 1.7 and 10.2, and its breakdown kinetics have been studied extensively across the corresponding pH ranges, showing that degradation increases by *ca.* 80 fold in alkaline media (correlated with the increased reactivity of the triplet state) until pH 10, when the anion is formed [4].

Unsurprisingly, the extensive solution-phase photochemical behavior of riboflavin has accrued much experimental attention over the years [1,5]; however, studies of its intrinsic (*i.e.*, gas-phase) excited-state properties, and those of other flavins, have been sparse until very recently [6–13].   To date, the only gas-phase study of a system involving riboflavin is that of Dopfer and co-workers on alkali metal coordination [9].   This situation is significant given the need for gas-phase studies as benchmarks for computational work.   For anionic flavin systems, Matthews *et al.* have compared the intrinsic electronic behavior of deprotonated LC and its related chromophore alloxazine (AL), finding novel near-threshold transient anion resonance states, which were assigned to dipole-bound excited states [6].   Recently, Bull *et al*. have utilized tandem ion mobility spectrometry and action spectroscopy to bring to light the influence that deprotonation sites have on the electronic absorption properties and photochemistry of the FAD anion [8], following on from earlier experimental work assigning probable sites of (de)protonation of flavins in the gas phase [9–14]. Non-statistical (*i.e.*, occurring during the excited-state lifetime) LC formation of the FAD mono-anion was found to proceed through a photo-induced intramolecular proton-coupled electron transfer of riboflavin [9].

In this article, we present the first UV-visible electronic gas-phase study of the deprotonated form of riboflavin. We employ the technique of gas-phase laser photodissociation

action spectroscopy on [RF–H]⁻ through forming the anion as an isolated gas-phase species *via* electrospray ionization (ESI), and then obtaining the electronic absorption spectrum and action spectra of its resultant photofragment ions. Our gas-phase measurements are complemented by on-line photolysis in a UV-LED photolytic cell (365 nm) with ESI mass spectrometry (ESI-MS) [15]. This experimental approach which characterizes the gas- and solution-phase behavior of a chosen system provides a "one-pot" tool for approaching the understanding photochemistry. The technique builds on other recent experiments which have employed on-line photolysis, with subsequent mass spectrometric detection [16–20]. The benefit of this approach is that the solution-phase measurements probe a more "real-world" environment for the riboflavin vitamin (*e.g.*, when it is in milk or within a cosmetic formulation), while the gas-phase measurements aid the understanding of the solution-phase photochemical mechanisms.   The solution-phase environment is potentially much more complex, since direct photoproducts can undergo secondary reactions and will be subject to environmental factors, *i.e.*, pH, solvent, and aggregation [5,16–20]. This two-step method provides a new approach that could be widely applied to characterize the photochemical breakdown of food, beauty, and pharmaceutical products.

2. Results

2.1. Gas-Phase Absorption Spectroscopy of [RF–H]⁻

Figure 1 shows the electrospray ionization mass spectrum of a solution of riboflavin obtained in negative ion mode. [RF–H]⁻ appears as the dominant ion in the mass spectrum, with *m/z* 375 (Figure 1), along with a second intense fragment ion with *m/z* 255 which can be assigned as deprotonated lumiflavin, [LF–H]⁻. (Intriguingly, its corresponding protonated species is not observed at all in positive ion mode; Section S5, Figure S9.) The dimer complex, *i.e.* [RF–H]⁻·RF is observed at *m/z* 751.
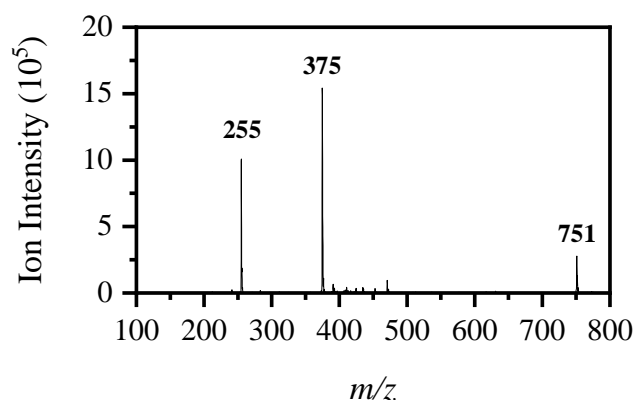

Figure 1. Negative ion mode ESI mass spectrum of deprotonated riboflavin ([RF–H]⁻).

Laser-interfaced mass spectrometry (LIMS) was used to characterize the wavelength-dependent photoabsorption and photofragmentation properties of [RF–H]⁻ *in vacuo*. The spectra are acquired by action spectroscopy, as described in Section 4 and in References [21–23]. Figure 2a displays the gas-phase photodepletion spectrum of [RF–H]⁻, which can be considered to be the gas-phase UV-visible absorption spectrum of the ion, subject to the limitations discussed in References [22,24–26]. The absorption spectrum displays an absorption onset at 2.0 eV (620 nm), followed by five bands labeled **I-V**. Bands **I-III** (at *ca.* 3.0, 3.5, and 4.2 eV, respectively) are medium intensity, broad bands, with band **I** observed in the visible region, centered around 3.0 eV (414 nm). Absorption continues to extend across into the UV-C region, where band **IV** appears as a relatively strong feature

between 4.5–5.2 eV, peaking at 5.0 eV (246 nm). The rising edge of band **V** is at the high-energy spectral edge and extends beyond 5.74 eV (216 nm).

The absorption profile of [RF–H]$^-$ in aqueous solution is shown in Figure 2b, for comparison with the gaseous spectrum (Figure 2a). RF has multiple acidic protons, and its reported pK_a values of 1.7 and 10.2 [27] indicate that it will be deprotonated in aqueous solution at neutral pH. Drössler *et al.* have demonstrated that the solution-phase UV absorption spectra of RF in aqueous solution is unchanged between the pH values of 7.0, 9.3, 10.25, and 13.35 [28].
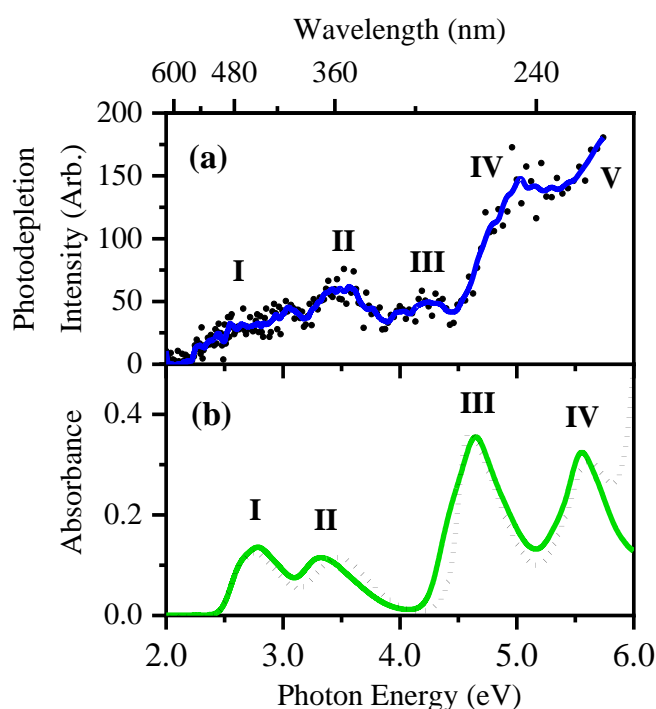
Figure 2. (a) Gas-phase photodepletion (absorption) spectrum of ([RF–H]$^-$) and **(b)** static solution-phase absorption spectrum of RF in aqueous solution (pH ~ 5.5; solid green line) and RF in aqueous solution with trace amounts of NH$_3$ (pH ~11.2; dotted black line).

On comparing the experimental gaseous and solution-phase spectra in Figures 2a and 2b, respectively, both spectra are seen to display relatively low absorption across the visible-UV-B regions, with the two dominant gas-phase UV bands (**IV** and **V**) likely to correspond to the strong **III** and **IV** features seen in the solution phase. It is striking that the intense solution-phase transition band **III** seems to appear much less strongly in the gas-phase spectrum (4.3 eV). This effect can arise from fluorescence decay of the electronic states associated bands which are not observed in the gas-phase when action spectroscopy is used to acquire the absorption spectrum [26]. Indeed, riboflavin is known to exhibit fluorescence, with its anionic form in particular, found to exhibit a fluorescence quantum yield of 1.2×10^{-3} in aqueous solution [28].

2.2. Gas-Phase Photofragmentation of [RF–H]$^-$

We next turn to exploring the gas-phase photofragment ions that are associated with the excited states evident in the gaseous absorption spectrum (Figure 2a). Figures 3a-e display the photofragment mass spectra of [RF–H]$^-$ obtained following excitation at 2.5, 3.5, 4.2, 4.7, and 5.0 eV. The spectra show that ions at *m/z* 255 and 241 are observed as the dominant and minor ionic fragments respectively, corresponding to a loss of 120 and 134 Da from [RF–H]$^-$ to form deprotonated lumiflavin ([LF–H]$^-$) and lumichrome ([LC–H]$^-$), respectively. It has been previously noted that both LF and LC are formed in alkaline media *via* the triplet excited state *via* formylmethylflavin (FMF; 284.27 Da), which

is believed to be an intermediate in the photolysis of RF. Several less intense, minor fragment ions are also observed, *e.g.*, at *m/z* 212 and 145.
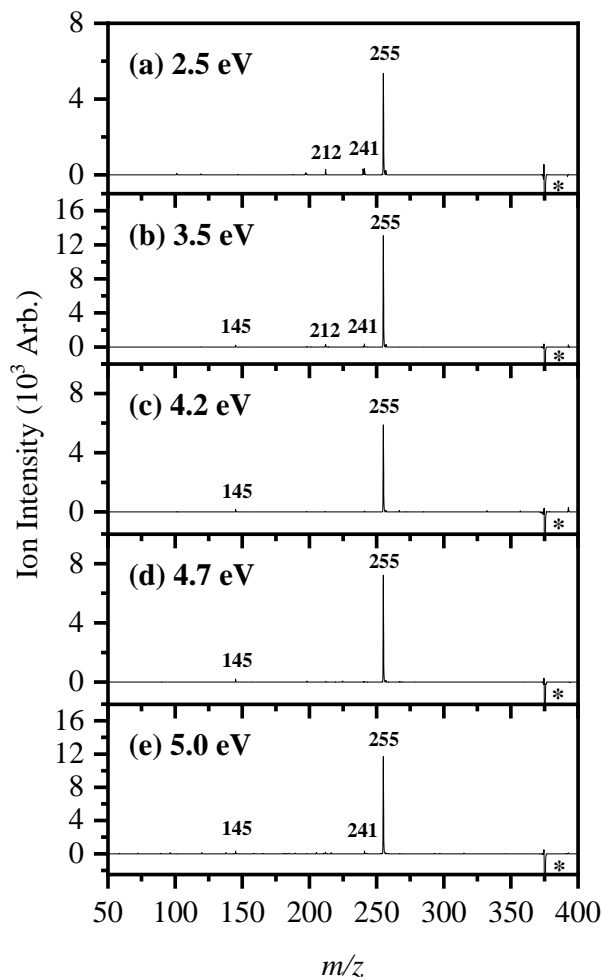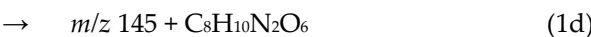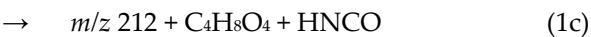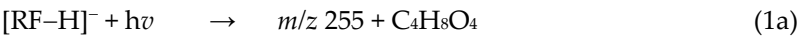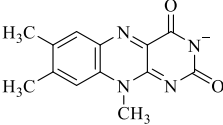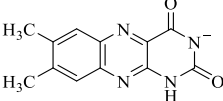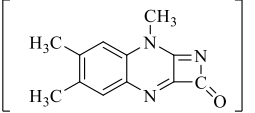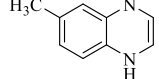

Figure 3. Photofragment difference (laser$_{ON}$ – laser$_{OFF}$) mass spectra of [RF–H]$^-$ excited at five photodepletion maxima of **(a)** 2.5, **(b)** 3.5, **(c)** 4.2, **(d)** 4.7, and **(e)** 5.0 eV. [*] indicates the photodepleted parent ion signal at *m/z* 375.

The major photodissociation channels are summarized in Equations (1a)-(1d) and again in Table 1.

$$[RF–H]^- + h\nu \quad \rightarrow \quad m/z\ 255 + C_4H_8O_4 \tag{1a}$$

$$\rightarrow \quad m/z\ 241 + C_5H_{10}O_4 \tag{1b}$$

$$\rightarrow \quad m/z\ 212 + C_4H_8O_4 + HNCO \tag{1c}$$

$$\rightarrow \quad m/z\ 145 + C_8H_{10}N_2O_6 \tag{1d}$$

Since [RF–H]$^-$ is anionic, any photodepletion that is not associated with photofragment ion production must generally be associated with electron loss processes [6,29,30]. This is discussed further in Section S2.

Table 1. Summary of the major ionic fragments of [RF–H]⁻ (*m/z* 375) observed upon collisional dissociation (CID), higher-collisional dissociation (HCD), gas-phase UV-visible laser photoexcitation, and solution-phase on-line UVA (365 nm) photolysis.

Ionic Fragment Mass (*m/z*)[1]	Proposed Structure of Fragment	Mass of Accompanying Neutral Mass Lost	Observed in CID (*via* H_2O)[1,2]	Observed in HCD (*via* EtOH)		Observed in Laser UV-visible Photoexcitation[1,2]	Observed *via* Solution-Phase On-line UV-A Photolysis[1,2]	
				25%	50%		3 min	6 min
255	*(structure: H₃C, H₃C, N, O, N⁻, O, N, CH₃)*	120	✓ (vs)	✓ (s)	✓ (m)	✓ (s)	✓ (w)[4]	✓ (vw)
241	*(structure: H₃C, H₃C, N, O, N⁻, O, N, H)*	134	-	-	✓ (w)	✓ (w)	✓ (w)	✓ (vs)
212	*(structure: CH₃, H₃C, H₃C, N, N, N⁻, C, O)*	163	-	✓ (w)	✓ (m)	✓ (w)	✓ (w)	✓ (w)
145	*(structure: H₃C, N⁻, N, H)*	230	-	✓ (w)	✓ (w)	✓ (w)	-	

[1] *Determined with mass accuracy > 0.3 amu.* [2] *very strong (vs), strong (s), medium (m), weak (w), and very weak (vw).* [3] *Fragment ions with masses above that of the parent ion at m/z 375 stem from that of the RF dimer complex (i.e., [RF–H]⁻·RF at m/z 751) and its photofragment (i.e., at m/z 617). The ion at m/z 617 results from the loss of 134 Da (C₅H₁₀O₄) from the dimer complex at m/z 751.* [4] *Notably, the ion at m/z 255 is thought to be produced via the ESI process of the aqueous RF or via means of in-source dissociation, and is thus intensely observed pre-irradiation.*

The novelty of our LIMS set-up allows us to monitor the photofragment production intensities at each scanned wavelength to provide further insight into the nature of the excited states. Figure 4b displays the production spectrum of the major photofragment [LF–H]⁻ with *m/z* 255, showing that it is produced across the entire experimental spectral range from 2.0–5.74 eV (620–216 nm), with significant peaks in production at the band maxima **I**-**V** of the gas-phase absorption spectrum of [RF–H]⁻ (Figure 4a for ease of comparison). The photofragment production spectra of the minor fragments at *m/z* 241 and 212 (Figures 4c and 4d, respectively) also display similar absorption maxima at 3.5, 5.0, and 5.7 eV, but with distinctive absorption profiles in the lower-energy region *ca.* 2.5 eV compared to the *m/z* 255 ion. Little to no production of these fragments occurs between 4.0-4.5 eV. The production spectrum of the *m/z* 145 photofragment (Figure 4e) has a production onset at ~2.75 eV, subsequently peaking at 3.25 eV, 5.0 and 5.7 eV.
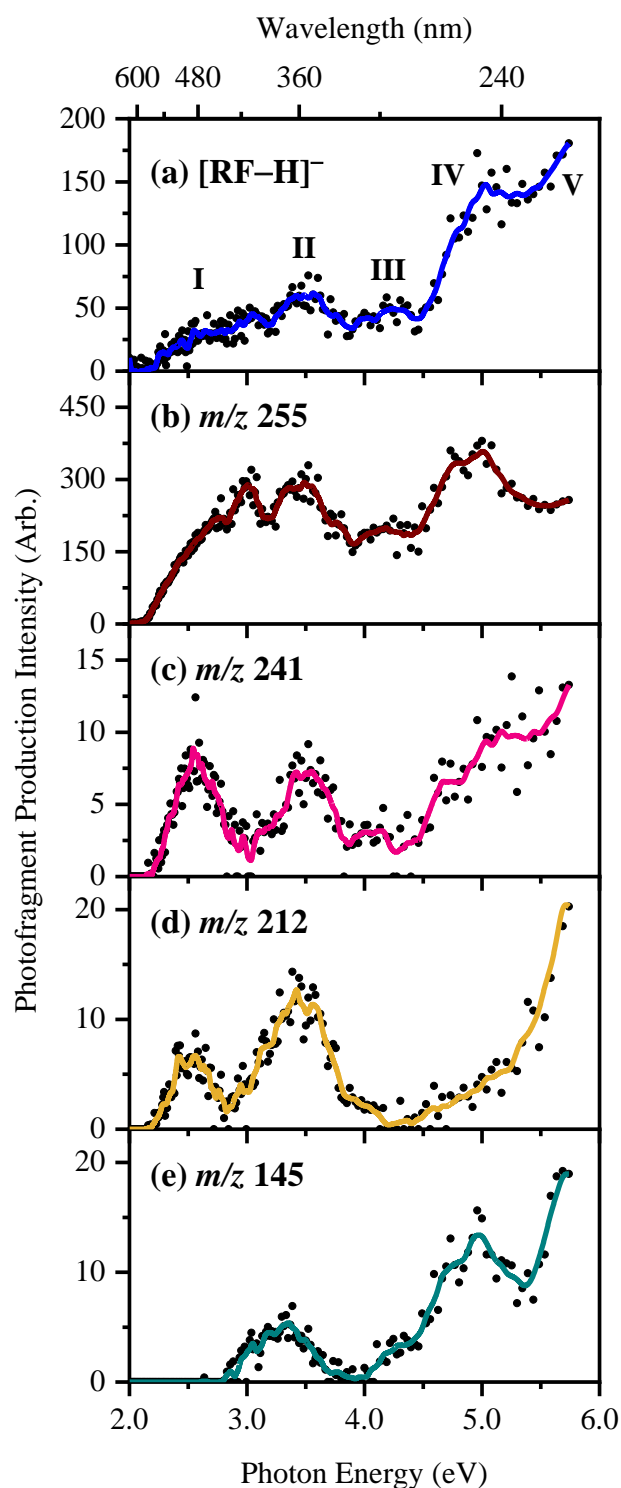
Figure 4. (a) Gas-phase photodepletion (absorption) spectrum of [RF−H]⁻ (*m/z* 375). **(b-e)** Photofragment production spectra of the four major [RF−H]⁻ photofragment ions at *m/z* 255, 241, 212, and 145, respectively. The solid line is a five-point adjacent average of the data points.

Figure 5 presents the relative photofragment ion yields for [RF−H]⁻ as a function of excitation energy, revealing several maxima that can be attributed to photoexcitation into different electronic states [31,32]. It is evident that between 2.0–3.0 eV, the *m/z* 241 and 212 photofragment ions are dominant, whereas the *m/z* 145 ion is not produced across this region. Between 3.0-4.0 eV, all three fragments are produced, with *m/z* 212 produced with

~50% greater intensity than that of the *m/z* 145 ion. In contrast, between 4.0–5.74 eV, *m/z* 145 overtakes both the *m/z* 241 and 212 ions in relative ion intensity, with all three increasing steadily with photon energy towards the high-energy edge.
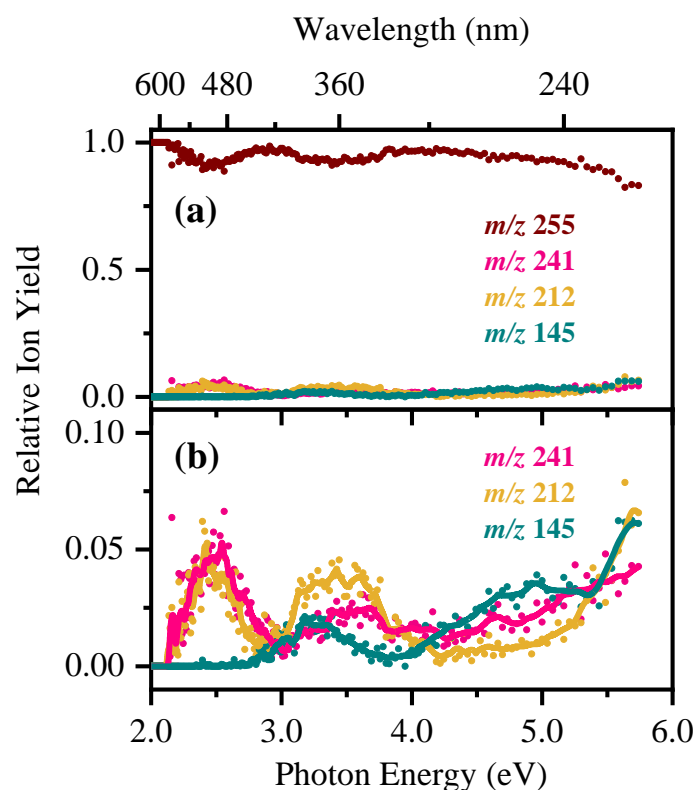

Figure 5. (a) Relative ion yield plot highlighting the relative ion yields of the 4 most dominant laser-induced [RF−H]⁻ photofragments at *m/z* 255, 241, 212, and 145 between 2.0–5.74 eV. **(b)** Zoomed-in view of the data presented in (a), providing a clearer view the ion yields of the *m/z* 241, 212, and 145 photofragment ions.

2.3. Collision-Induced Dissociation of [RF−H]⁻

Low-energy collision-induced dissociation (CID) of [RF−H]⁻ gives [LF−H]⁻ (*m/z* 255) as the only ionic product (Figure 6). The CID process is equivalent to thermal heating of ground state [RF−H]⁻, with subsequent fragmentation across the lowest energy fragmentation barrier on the ground state surface [33]. The precursor [RF−H]⁻ ion does not dissociate up to ~40% CID, indicating that the ion is stable against spontaneous dissociation. However, as noted in Section 2.1, ESI-MS of riboflavin produces *m/z* 255 as well as [RF−H]⁻, and the observation of *m/z* 255 as a CID fragment indicates that [RF−H]⁻ is likely fragmenting into *m/z* 255 either during ESI or *via* in-source dissociation. It is also notable that *m/z* 255 is the major gas-phase laser photofragment ion.
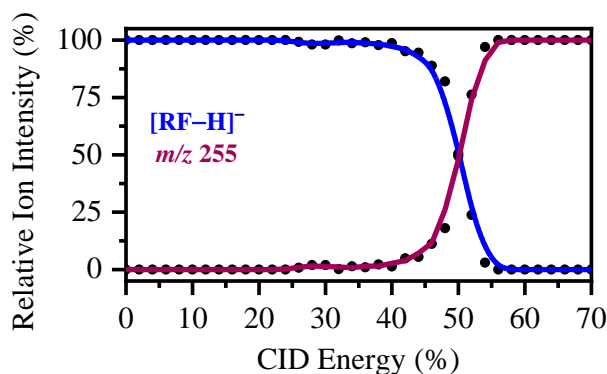
Figure 6. Low-energy collision-induced dissociation (CID) fragmentation decay curve for [RF–H]⁻ (*m/z* 375) upon CID between 0-70% CID energy. The curved lines included with the data points are a three-point adjacent average of such data points.

To further probe the thermal fragmentation pathway(s) of [RF–H]⁻ on its electronic ground state, higher-energy collisional dissociation (HCD) was employed. These measurements are ideal to identify which ions are secondary fragments, formed when a precursor (or intermediate) species fragments at high internal energy. Importantly, any photofragments not observed in these HCD experiments can be identified as purely photochemical products. A HCD plot of [RF–H]⁻ electrosprayed in EtOH in the negative ion mode is shown in Figure 7, revealing the nature of the thermal degradation products at higher HCD energies. (We note that it was not possible to electrospray from an aqueous solution in these experiments, due to differences in the ionization efficiencies of the two different instruments used.). However, it was possible to electrospray from both EtOH and MeCN in the HCD instrument. The results obtained with both solvents were extremely similar, giving us confidence that this would also be the case if the electrospray had been conducted from an aqueous solution.)

At relatively low collisional energies (0–25% HCD), the most intense fragment ion is *m/z* 255, with *m/z* 243 peaking at ~15% higher relative ion intensity. Production of the *m/z* 255 ion gradually decreases beyond 25% HCD energy, where the onset of the *m/z* 212 ion occurs. This secondary ion subsequently peaks at 48% HCD energy. However, since the *m/z* 255 fragment clearly dominates in both the gas-phase laser and thermal (*i.e.*, CID and HCD) fragmentation experiments, photofragmentation of [RF–H]⁻ can be categorized as predominantly statistical (ergodic) over the spectral range of this experiment [31,34].
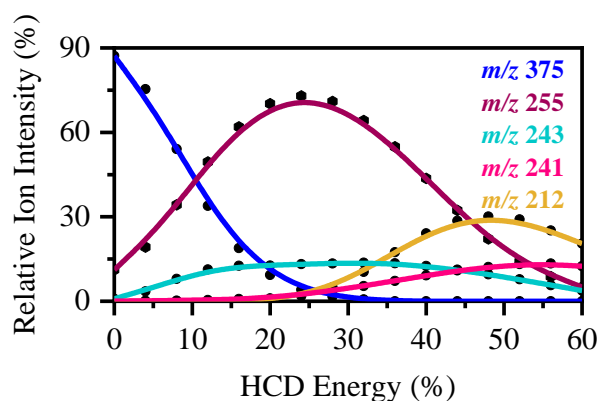

Figure 7. Parent ion dissociation curves [RF–H]⁻ (*m/z* 375) and its four most intense thermal fragments between 0% and 60% HCD energy, as electrosprayed in EtOH. The curved lines are a five-point adjacent average of such data points and are provided as a viewing guide, to emphasize the each fragment's profile. Section S3 presents complete HCD data for the minor fragments.

Overall, the CID and HCD fragmentation experiments reveal that [RF–H]$^-$ primarily dissociates into the m/z 255 ion, which subsequently dissociates into m/z 212 at higher internal energy, and increasingly into m/z 241 and 145 at the highest internal energies.

2.5 On-Line Solution-Phase Photolysis of [RF–H]$^-$

Figure 8 shows photolysis$_{ON}$ – photolysis$_{OFF}$ (difference) ESI mass spectrum obtained from the photolysis (UV-A; 365 nm) of aqueous riboflavin at 3, 6, 9, and 12 minutes. The [RF-H]$^-$ precursor ion (m/z 375), the primary thermal ion (m/z 255), and the dimer ion (m/z 751) are all seen to be depleted in the difference spectra, indicating that they are photolyzed at this wavelength. Solution-phase photolysis of [RF–H]$^-$ dominantly produces the same m/z 241 ion that was observed in the gas-phase irradiation experiments, which corresponds to the production of [LC–H]$^-$. The ion at m/z 617 is again the loss of $C_5H_{10}O_4$ (134 Da) from the dimer complex [RF–H]$^-\cdot$RF at m/z 751. The same loss in m/z is observed in Eq. 1b.
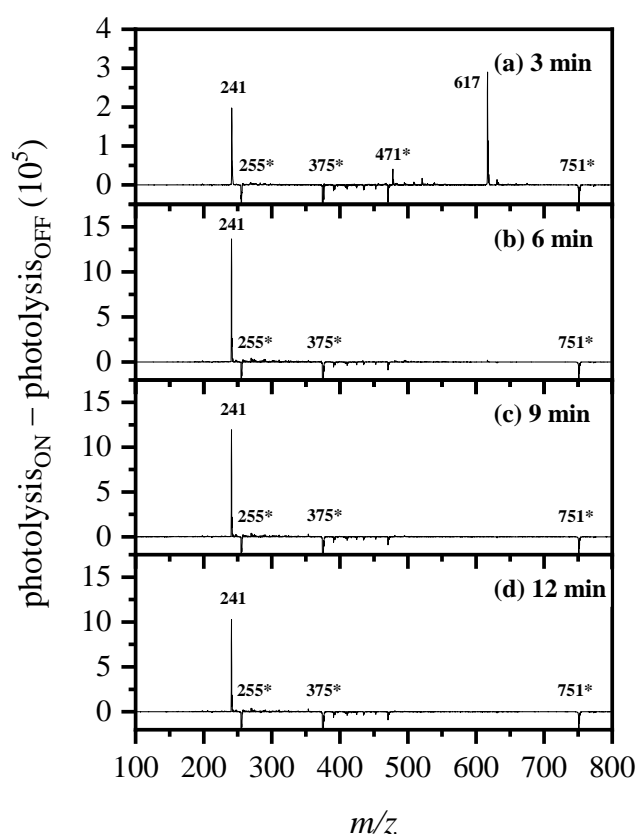

Figure 8. (a) Photolysis$_{ON}$ – photolysis$_{OFF}$ ESI mass spectra of a solution of aqueous RF after irradiation at 365 nm (3.4 eV) at 3, 6, 9, and 12 min. [*] indicates the photodepleted ions at m/z 255, 375, 471, and 751, where m/z 375 is that of the parent ion.

Figure 9 shows the relative ion intensities of the solution-phase photofragment ions observed through ESI-MS as a function of irradiation time. The relative intensities of the ions which are initially present upon electrospray (*i.e.*, m/z 255, 375, and 751) remained steady until *ca.* 3.0 min (the transit time of the solution that is being photolyzed into the MS), where the sudden production onset of the major m/z 241 fragment ion is then observed. Several relatively minor fragments (<5% relative ion intensity over 30 min of irradiation) are also observed, as outlined in Figure S4.
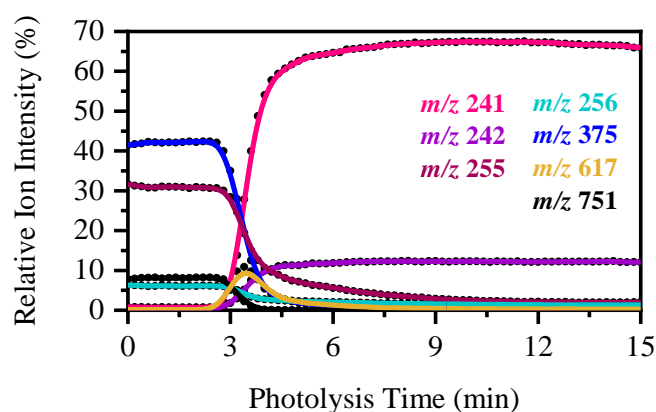
Figure 9. Relative ion intensity plot highlighting the solution-phase photofragment ions of aqueous [RF–H]⁻ produced over a 15-minute interval of irradiation at 365 nm (3.4 eV) when delivered *via* ESI-MS in the negative ion mode. The curved lines included with the data points are a three-point adjacent average of such data points and are extracted from an average of 3 repeat runs. The production curves of the minor solution-phase photofragments are illustrated in Figure S4.

Control experiments run in parallel using routine ESI-MS detection showed that under the same photolytic conditions, solutions of [RF–H]⁻ held within "black-coated" syringes (*e.g.*, to block all transmission of UV light) showed no degradation of the parent (*m/z* 375) ion, nor the *m/z* 255, or *m/z* 375 ions (see Section S6; Figures S10 and S11). The solution-phase photofragment at *m/z* 241 identified earlier in Figures 8 and 9 was also not observed. This demonstrated that these ions remained unaffected by any several external factors (*e.g.*, heating or hydrolysis).

3. Discussion

In this work, gas-phase laser-interfaced photodissociation mass spectrometry has been employed on the native form of riboflavin for the first time to map its intrinsic UV-visible absorption (photodepletion) spectrum and associated photodegradation products. Solution-phase photoproducts were generated *via* photolysis on-line with the MS instrument, and were characterized using ESI-MS and compared with the gas-phase results. Whilst [RF–H]⁻ was found to photodegrade into deprotonated lumichrome (*m/z* 241) *via* the loss of 134 Da in both the gas and solution phase at 365 nm (3.4 eV), further ions at *m/z* 255, 212, and 145 were observed to be produced following gas-phase photodissociation of the isolated molecular ion. (Our HCD results revealed that the *m/z* 255 ion dissociates into *m/z* 212 and 145 at high internal energies.)

The photoproducts observed in this work mirror those seen in related work by Insińska-Rak *et al*. [17,20], where pH neutral solutions of riboflavin and its derivatives were photolyzed by mercury lamps, and photoproducts detected by HPLC and electron ionization mass spectrometry (EI-MS). The EI-MS fragmentation pathways of riboflavin proceed with *via* formation of lumichrome and lumiflavin, with major ions observed at *m/z* 256 (relative intensity of 33%), 213 (43%), 198 (52%), and 170 (25%) *via* the lumiflavin route, or *m/z* 242 (12%), 199 (28%), 171 (42%), and 156 (16%) through the lumichrome route [17,20]. (Note that such mass-to-charge ratios are monitored *via* EI-MS). All of the photofragments observed in the work of Insińska-Rak *et al*. are in line with the main photoproducts formed in this work (with the exception of our *m/z* 145 photofragment, which we know is a secondary fragment).

The results presented herein therefore demonstrate an elegant new technique for monitoring solution-phase photodegradation of [RF–H]⁻ and detection of its resulting ionic photodissociation products. The direct and uninterrupted injection of the irradiated contents of the syringe allows for continuous real-time monitoring of the change in ion

intensities of select ions over time (see Figure 9). This work also demonstrates the value of performing the gas-phase photodissociation measurements, even in the absence of on-line solution-phase photolysis, since the gas-phase measurement allows the identification of the major photolysis product for this system, and hence potentially others. The gas-phase measurements have several advantages as they are conducted against zero back-ground, hence allowing straightforward identification of minor photoproducts, as well as allowing the primary photoproducts to be identified away from secondary reactions that can occur in solution. Nonetheless, the combination of on-line solution-phase photolysis coupled with gas-phase photolysis of the mass-selected species of interest clearly allows a rapid and straightforward link to be established between the gas-phase measurement and the "real world" environment of the solution photochemistry. This approach has potential for widespread application across photochemical systems of interest, including photopharmaceuticals [35] and sunscreens [23,36,37].

4. Materials and Methods

Laser-Interfaced Photodissociation Mass Spectrometry. The gaseous ion absorption (photodepletion) and photofragment production spectra of [RF–H]⁻ were recorded *in vacuo* using laser action spectroscopy. An AmaZon SL mass spectrometer (Bruker Daltonics Inc., Billerica, MA, USA), modified for laser-interfaced mass spectrometry (LIMS), was used as described previously. RF was purchased from Sigma-Aldrich (St. Louis, MA, USA) and used as received. RF solutions (1×10^{-5} M) in deionized H_2O were electrosprayed at a capillary temperature 100 °C in the negative ion mode. Trace amounts of NH_3 (0.4%) was added to the aqueous solution(s) to aid the electrospray process, as the intensity of ions produced without the additive deemed insufficient for later gas-phase measurements.

[RF–H]⁻ was mass-selected (*m/z* 375) and isolated in the ion trap prior to laser irradiation. Photons were produced by an Nd:YAG pumped OPO laser (Surelite™/Horizon™, Amplitude Laser Group, San Jose, CA, USA), giving 0.1 ± 15% mJ across the UV-visible range 620-216 nm (2.0-5.74 eV), with 2 nm laser step sizes in the UV and 4 nm steps in the visible. Photofragmentation experiments were conducted with an ion accumulation time of 20 ms. To minimize the possibility of multiphoton events *via* sequential absorption, each mass-selected ion packet interacts with only one laser pulse (corresponding to a fragmentation time of 100 ms), and photodepletion restricted to ~40 % of the precursor ion at the wavelength of maximum absorption. Multiphoton events *via* instantaneous absorption of multiple photons in the Franck-Condon region are negligible as the laser beam is only softly focused through the ion-trap region.

Photodepletion of [RF–H]⁻ was measured as a function of the scanned wavelength, with photofragment production recorded simultaneously [Eq. (2)-(4)]:

$$\text{Photodepletion (PD) Intensity} = \frac{\ln\left(\frac{\text{Int}_{OFF}}{\text{Int}_{ON}}\right)}{\lambda \times P} \tag{2}$$

$$\text{Photofragment (PF) Production Intensity} = \frac{\left(\frac{\text{Int}_{FRAG}}{\text{Int}_{OFF}}\right)}{\lambda \times P} \tag{3}$$

$$\text{Relative Ion Yield} = \frac{\text{Int}_{FRAG}}{\text{Int}_{PFT}} \tag{4}$$

In these expressions, Int_{OFF} and Int_{ON} are the laser off and on parent ion peak intensities respectively; Int_{FRAG} is the fragment intensity with the laser on; λ is the excitation wavelength (nm); P is the laser pulse energy (mJ); and Int_{PFT} is the sum of the photofragment

ion intensities with the laser on. The photodepletion spectrum is considered to be equivalent to the gaseous absorption spectrum in the limit where excited state fluorescence is negligible.

Electron detachment yield (ED*) spectra were calculated by assuming that any depleted ions not detected as ionic photofragments are decaying *via* means of electron detachment, as determined using Eq. 5. This analysis assumes that both the parent ions and photofragments are detected equally in the mass spectrometer. In Figure S2 where we present ED* spectra, we overlay such data with the photodepletion yield (PD*). PD* is the normalized photodepletion ion count (Eq. 6), which provides the most straightforward comparison to the electron detachment yield (Eq. 5).

$$\text{Electron detachment yield (ED*)} = \frac{\frac{(\text{Int}_{\text{OFF}} - \text{Int}_{\text{ON}}) - \text{Int}_{\text{PFT}}}{\text{Int}_{\text{OFF}}}}{\lambda \times P} \qquad (5)$$

$$\text{Photodepletion yield (PD*)} = \frac{\frac{\text{Int}_{\text{OFF}} - \text{Int}_{\text{ON}}}{\text{Int}_{\text{OFF}}}}{\lambda \times P} \qquad (6)$$

Analysis. Photodepletion intensities were taken from an average of three repeat runs at each wavelength of the range studied. We note that fragment ions with $m/z < 50$ are not detectable in our mass spectrometer since low masses fall outside the ion-trap mass window.

Collision-Induced Dissociation Energy. Low-energy collision-induced dissociation (CID) was performed to investigate the ground-state thermal fragmentation characteristics of [RF–H]⁻, using the aforementioned Bruker AmaZon mass spectrometer. Here, an excitation AC folder was applied to the end caps of the ion trap to induce low-energy collisions of the trapped anions with the helium buffer gas, as has been described in detail previously [33,38]. Precursor ion excitation within the quadrupole ion trap occurs through multiple low-energy collisions with helium. Resonance excitation amplitudes for thermal decomposition of molecular ions within a quadrupole ion trap have been shown to correlate with literature critical dissociation energies. However, given that is no direct conversion from the resonance excitation voltage to absolute CID energies, such CID energies are therefore quoted as a percentage of the 2.5 V excitation voltage, in line with other standard practices [33,38–40].

Higher-energy Collisional Dissociation. Higher-energy collisional dissociation (HCD) was performed on [RF–H]⁻, electrosprayed from solutions of EtOH and MeCN using an Orbitrap Fusion Tribid mass spectrometer (Thermo Fisher Scientific, Waltham, MA, USA) with an ESI source, run in the negative ion mode between 0% and 60% collisional energy. This technique provides tandem mass spectrometry and was operated at a flow rate of 3.0 µL/min, with the following parameters: spray voltage: -2000 V; sheath gas flow rate: 10; aux. gas flow rate: 2.0; ion transfer tube temperature: 290 °C; vaporizer temperature: 20 °C; MS² detector: Orbitrap; scan rate: enhanced; MS² injection time: 100 ms; and RF lens: 60%.

Solution-Phase UV-A Photodissociation. For sample irradiation, four UV-A light emitting diodes (LEDs; 365 nm {3.4 eV}, LZ1-00UV00, LED Engin, Inc., San Jose, CA, USA) were employed. The four LEDs were connected in series and powered with a 500 mA constant current power source. Each of the LEDs were situated onto each face of the square (23 mm × 23 mm) interior of the custom designed aluminum cell, surrounding the barrel of the UV-transmitting borosilicate glass of the syringe (model 1002LTN; 2.5 mL; needle size: 22 ga [blunt tip]; needle length: 51 mm; Hamilton®, Reno, Nevada, USA). A syringe-pump set to inject solution at 0.33 mL/hr was fitted to hold the cell and syringe, allowing for direct on-line measurement of the contents *via* ESI-MS (see Section S5). The design of the cell allows for a designated volume (*i.e.*, >2.5 mL) of the contents of the syringe to be continually irradiated in chorus for a set time (*i.e.*, 15 minutes). The cell is

adapted to permit greater volumes of solution(s), and thus alternate syringes, to be continuously irradiated. A fitted shield has also been added to protect the contents of the syringe from latent photodegradation resulting from that of standard laboratory lighting.

The stability of all RF solutions involved were also monitored *via* static solution-phase UV-visible absorption spectroscopy over a 4-hour window (See Section S5; Figure S6). Similarly, as depicted in Figures S7 and S8, static UV-visible absorption spectra of the irradiated aqueous RF samples (with/without NH_3, respectfully) were taken by manually transferring the irradiated solution(s) from the syringe in which the solution(s) were irradiated in (model 1002LTN; 2.5 mL; Hamilton®) into a far-UV quartz (macro)cuvette (10 mm pathlength; Hellma® UK Ltd., Essex, UK) for measurement *via* a conventional spectrophotometer (GENESYS 180; Thermo Fisher Scientific, Waltham, MA, USA). Notably, deionized H_2O was used as the baseline solvent, with solutions being irradiated in 1-minute intervals up to 20 minutes.

To differentiate any photoproducts from that of any consequential potential thermal (*i.e.*, heat) products generated from the array of LEDs, an opaque black cloth was wrapped around the fitted syringe in a separate set of studies (see Section S5; Figures S10 and S11), to remove the influence of the UV-A light from the LEDs, with a temperature probe fitted to review the temperature of the experiment over time (Figure S12).

To mirror the deprotonated solutions used for gas-phase LIMS, on-line solution-phase UV photodissociation was primarily carried out on aqueous RF with NH_3 (0.4%). But for completeness, the solution-phase experiments were comprehensively repeated with and without the influence of NH_3. High-resolution measurements were additionally performed on a Thermo Fisher Orbitrap mass spectrometer to allow for adequate differentiation of any (photo/thermal) product ions from that of contaminants typically found in the negative ion mode. Further analysis of the high-resolution monitoring of the reaction(s) is available within Section S6.

Conflicts of Interest: The authors declare no conflict of interest.

References

1.   Sheraz, M.A.; Kazi, S.H.; Ahmed, S.; Anwar, Z.; Ahmad, I. Photo, thermal and chemical degradation of riboflavin. *Beilstein J. Org. Chem.* **2014**, *10*, 1999–2012, doi:10.3762/bjoc.10.208.

2.   Ahmad, I.; Mirza, T.; Musharraf, S.G.; Anwar, Z.; Sheraz, M.A.; Ahmed, S.; Ejaz, M.A.; Khurshid, A. Photolysis of carboxymethylflavin in aqueous and organic solvent: a kinetic study. *RSC Adv.* **2019**, *9*, 26559–26571, doi:10.1039/C9RA02818H.

3.   Knak, A.; Regensburger, J.; Maisch, T.; Bäumler, W. Exposure of vitamins to UVB and UVA radiation generates singlet oxygen. *Photochem. Photobiol. Sci.* **2014**, *13*, 820–829, doi:10.1039/C3PP50413A.

4.   Ahmad, I.; Fasihullah, Q.; Noor, A.; Ansari, I.A.; Ali, Q.N.M. Photolysis of riboflavin in aqueous solution: a kinetic study. *Int. J. Pharm.* **2004**, *280*, 199–208, doi:10.1016/j.ijpharm.2004.05.020.

5.   Astanov, S.K.; Kasimova, G.K.; Kurtaliev, E.N.; Nizomov, N.N.; Jumabaev, A. Electronic nature and structure of aggregates of riboflavin molecules. *Spectrochim. Acta Part A Mol. Biomol. Spectrosc.* **2021**, *248*, 119177, doi:10.1016/j.saa.2020.119177.

6.   Matthews, E.; Dessent, C.E.H. Observation of Near-Threshold Resonances in the Flavin Chromophore Anions Alloxazine and Lumichrome. *J. Phys. Chem. Lett.* **2018**, *9*, 6124–6130, doi:10.1021/acs.jpclett.8b02529.

7.   Matthews, E.; Cercola, R.; Dessent, C. Protomer-Dependent Electronic Spectroscopy and Photochemistry of the Model Flavin Chromophore Alloxazine. *Molecules* **2018**, *23*, 2036, doi:10.3390/molecules23082036.

8.   Bull, J.N.; Carrascosa, E.; Giacomozzi, L.; Bieske, E.J.; Stockett, M.H. Ion mobility action spectroscopy of flavin dianions reveals deprotomer-dependent photochemistry. *Phys. Chem. Chem. Phys.* **2018**, *20*, 19672–19681, doi:10.1039/c8cp03244k.

9.   Stockett, M.H. Photo-induced proton-coupled electron transfer and dissociation of isolated flavin adenine dinucleotide mono-anions. *Phys. Chem. Chem. Phys.* **2017**, *19*, 25829–25833, doi:10.1039/C7CP04068G.

10.   Günther, A.; Nieto, P.; Müller, D.; Sheldrick, A.; Gerlich, D.; Dopfer, O. BerlinTrap: A new cryogenic 22-pole ion trap spectrometer. *J. Mol. Spectrosc.* **2017**, *332*, 8–15, doi:10.1016/j.jms.2016.08.017.

11.   Langer, J.; Günther, A.; Seidenbecher, S.; Berden, G.; Oomens, J.; Dopfer, O. Probing protonation sites of isolated flavins using IR spectroscopy: From lumichrome to the cofactor flavin mononucleotide. *ChemPhysChem* **2014**, *15*, 2550–2562, doi:10.1002/cphc.201402146.

12.   Zhang, T.; Papson, K.; Ochran, R.; Ridge, D.P. Stability of Flavin Semiquinones in the Gas Phase: The Electron Affinity, Proton Affinity, and Hydrogen Atom Affinity of Lumiflavin. *J. Phys. Chem. A* **2013**, *117*, 11136–11141, doi:10.1021/jp406786a.

13.   Guyon, L.; Tabarin, T.; Thuillier, B.; Antoine, R.; Broyer, M.; Boutou, V.; Wolf, J.-P.; Dugourd, P. Femtosecond pump-probe experiments on trapped flavin: Optical control of dissociation. *J. Chem. Phys.* **2008**, *128*, 075103, doi:10.1063/1.2828558.

14.   Sheldrick, A.; Müller, D.; Günther, A.; Nieto, P.; Dopfer, O. Optical spectroscopy of isolated flavins: Photodissociation of protonated lumichrome. *Phys. Chem. Chem. Phys.* **2018**, *20*, 7407–7414, doi:10.1039/c8cp00590g.

15.   Cercola, R.; Wong, N.G.K.; Rhodes, C.; Olijnyk, L.; Mistry, N.S.; Hall, L.M.; Berenbeim, J.A.; Lynam, J.M.; Dessent, C.E.H. A "one pot" mass spectrometry technique for characterizing solution- and gas-phase photochemical reactions by electrospray mass spectrometry. *RSC Adv.* **2021**, *11*, 19500–19507, doi:10.1039/D1RA02581C.

16.   Mehara, J.; Roithová, J. Identifying reactive intermediates by mass spectrometry. *Chem. Sci.* **2020**, *11*, 11960–11972, doi:10.1039/D0SC04754F.

17.   Insińska-Rak, M.; Prukała, D.; Golczak, A.; Fornal, E.; Sikorski, M. Riboflavin degradation products; combined photochemical and mass spectrometry approach. *J. Photochem. Photobiol. A Chem.* **2020**, *403*, 112837, doi:10.1016/j.jphotochem.2020.112837.

18.   Pahl, M.; Mayer, M.; Schneider, M.; Belder, D.; Asmis, K.R. Joining Microfluidics with Infrared Photodissociation: Online Monitoring of Isomeric Flow-Reaction Intermediates. *Anal. Chem.* **2019**, *91*, 3199–3203, doi:10.1021/acs.analchem.8b05532.

19.   Chen, S.; Wan, Q.; Badu-Tawiah, A.K. Picomole-Scale Real-Time Photoreaction Screening: Discovery of the Visible-Light-Promoted Dehydrogenation of Tetrahydroquinolines under Ambient Conditions. *Angew. Chemie Int. Ed.* **2016**, *55*, 9345–9349, doi:10.1002/anie.201603530.

20.   Insińska-Rak, M.; Golczak, A.; Sikorski, M. Photochemistry of riboflavin derivatives in methanolic solutions. *J. Phys. Chem. A* **2012**, *116*, 1199–1207, doi:10.1021/jp2094593.

21.   Matthews, E.; Dessent, C.E.H. Locating the proton in nicotinamide protomers via low-Resolution UV action spectroscopy of electrosprayed solutions. *J. Phys. Chem. A* **2016**, *120*, 9209–9216, doi:10.1021/acs.jpca.6b10433.

22.   Matthews, E.; Sen, A.; Yoshikawa, N.; Bergström, E.; Dessent, C.E.H. UV laser photoactivation of hexachloroplatinate bound to individual nucleobases: In vacuo as molecular level probes of a model photopharmaceutical. *Phys. Chem. Chem. Phys.* **2016**, *18*, 15143–15152, doi:10.1039/c6cp01676f.

23.   Wong, N.G.K.; Berenbeim, J.A.; Hawkridge, M.; Matthews, E.; Dessent, C.E.H. Mapping the intrinsic absorption properties and photodegradation pathways of the protonated and deprotonated forms of the sunscreen oxybenzone. *Phys. Chem. Chem. Phys.* **2019**, *21*, 14311–14321, doi:10.1039/C8CP06794E.

24.   Sen, A.; Luxford, T.F.M.; Yoshikawa, N.; Dessent, C.E.H. Solvent evaporation versus proton transfer in nucleobase–Pt(CN)4,62− dianion clusters: a collisional excitation and electronic laser photodissociation spectroscopy study. *Phys. Chem. Chem. Phys.* **2014**, *16*, 15490–15500, doi:10.1039/c4cp00989d.

25.   Antoine, R.; Dugourd, P. Visible and ultraviolet spectroscopy of gas phase protein ions. *Phys. Chem. Chem. Phys.* **2011**, *13*, 16494–16509, doi:10.1039/c1cp21531k.

26.   Wellman, S.M.; Jockusch, R.A. Moving in on the Action: An Experimental Comparison of Fluorescence Excitation and Photodissociation Action Spectroscopy. *J. Phys. Chem. A* **2015**, *119*, 6333–6338, doi:10.1021/acs.jpca.5b04835.

27.   O'Neil, M.J. The Merck Index, 15th edition.

28.   Drössler, P.; Holzer, W.; Penzkofer, A.; Hegemann, P. pH dependence of the absorption and emission behaviour of riboflavin in aqueous solution. *Chem. Phys.* **2002**, *282*, 429–439, doi:10.1016/S0301-0104(02)00731-0.

29.   Matthews, E.; Cercola, R.; Mensa-Bonsu, G.; Neumark, D.M.; Dessent, C.E.H. Photoexcitation of iodide ion-pyrimidine clusters above the electron detachment threshold: Intracluster electron transfer versus nucleobase-centred excitations. *J. Chem. Phys.* **2018**, *148*, 084304, doi:10.1063/1.5018168.

30.   Wong, N.G.K.; Rankine, C.D.; Dessent, C.E.H. Measurement of the Population of Electrosprayed Deprotomers of Coumaric Acids Using UV-Vis Laser Photodissociation Spectroscopy. *J. Phys. Chem. A* **2021**, *XXX*, XXX–XXX, doi:10.1021/acs.jpca.1c04880.

31.   Wong, N.G.K.; Rankine, C.D.; Dessent, C.E.H. Linking Electronic Relaxation Dynamics and Ionic Photofragmentation Patterns for the Deprotonated UV Filter Benzophenone-4. *J. Phys. Chem. Lett.* **2021**, *12*, 2831–2836, doi:10.1021/acs.jpclett.1c00423.

32.   Berenbeim, J.A.; Wong, N.G.K.; Cockett, M.C.R.; Berden, G.; Oomens, J.; Rijs, A.M.; Dessent, C.E.H. Unravelling the Keto–Enol Tautomer Dependent Photochemistry and Degradation Pathways of the Protonated UVA Filter Avobenzone. *J. Phys. Chem. A* **2020**, *124*, 2919–2930, doi:10.1021/acs.jpca.0c01295.

33.   Boxford, W.E.; Dessent, C.E.H. Probing the intrinsic features and environmental stabilization of multiply charged anions. *Phys. Chem. Chem. Phys.* **2006**, *8*, 5151–5165, doi:10.1039/b609123g.

34.   Cercola, R.; Matthews, E.; Dessent, C.E.H. Photoexcitation of Adenosine 5'-Triphosphate Anions in Vacuo: Probing the Influence of Charge State on the UV Photophysics of Adenine. *J. Phys. Chem. B* **2017**, *121*, 5553–5561, doi:10.1021/acs.jpcb.7b03435.

35.   Furlan, C.; Berenbeim, J.A.; Dessent, C.E.H. Photoproducts of the Photodynamic Therapy Agent Verteporfin Identified via

Laser Interfaced Mass Spectrometry. *Molecules* **2020**, *25*, 5280, doi:10.3390/molecules25225280.

36. Wong, N.G.K.; Berenbeim, J.A.; Dessent, C.E.H. Direct Observation of Photochemical Free Radical Production from the Sunscreen 2-Phenylbenzimidazole-5-Sulfonic Acid via Laser-Interfaced Mass Spectrometry. *ChemPhotoChem* **2019**, *3*, 1231–1237, doi:10.1002/cptc.201900149.

37. Berenbeim, J.A.; Wong, N.G.K.; Cockett, M.C.R.; Berden, G.; Oomens, J.; Rijs, A.M.; Dessent, C.E.H. Sodium cationization can disrupt the intramolecular hydrogen bond that mediates the sunscreen activity of oxybenzone. *Phys. Chem. Chem. Phys.* **2020**, *22*, 19522–19531, doi:10.1039/D0CP03152F.

38. Luxford, T.F.M.M.; Milner, E.M.; Yoshikawa, N.; Bullivant, C.; Dessent, C.E.H. Complexation of carboxylate anions with the arginine gas-phase amino acid: Effects of chain length on the geometry of extended ion binding. *Chem. Phys. Lett.* **2013**, *577*, 1–5, doi:10.1016/j.cplett.2013.05.040.

39. Zhang, J.; Brodbelt, J.S.; Wang, J. Threshold dissociation and molecular modeling of transition metal complexes of flavonoids. *J. Am. Soc. Mass Spectrom.* **2005**, *16*, 139–151, doi:10.1016/j.jasms.2004.10.005.

40. Wan, K.X.; Gross, M.L.; Shibue, T. Gas-phase stability of double-stranded oligodeoxynucleotides and their noncovalent complexes with DNA-binding drugs as revealed by collisional activation in an ion trap. *J. Am. Soc. Mass Spectrom.* **2000**, *11*, 450–457, doi:Doi 10.1016/S1044-0305(00)00095-7.